Structural, vibrational, and electrical properties of $1T$-$TiTe_2$ under hydrostatic pressure: Experiments and theory

V. Rajaji,[1] Utpal Dutta,[2] P. C. Sreeparvathy,[3] Saurav Ch. Sarma,[4] Y. A. Sorb,[1] B. Joseph,[5] Subodha Sahoo,[2] Sebastian C. Peter,[4] V. Kanchana,[3] and Chandrabhas Narayana[1,*]

[1]*Chemistry and Physics of Materials Unit, Jawaharlal Nehru Centre for Advanced Scientific Research, Jakkur P.O., Bangalore 560 064, India*
[2]*HP&SRPD, Bhabha Atomic Research Centre, Trombay, Mumbai 400 085, India*
[3]*Department of Physics, Indian Institute of Technology, Hyderabad, Kandi, Sangareddy 502285, Telangana, India*
[4]*New Chemistry Unit, Jawaharlal Nehru Centre for Advanced Scientific Research, Jakkur P.O., Bangalore 560 064, India*
[5]*Elettra Sincrotrone Trieste, S.S. 14, Km 163.5 in Area Science Park, Basovizza, Trieste 34012, Italy*

(Received 4 September 2017; published 5 February 2018)

We report the structural, vibrational, and electrical transport properties up to ~16 GPa of $1T$-$TiTe_2$, a prominent layered 2D system. We clearly show signatures of two isostructural transitions at ~2 GPa and ~4 GPa obtained from the minima in c/a ratio concomitant with the phonon linewidth anomalies of E_g and A_{1g} modes around the same pressures, providing a strong indication of unusual electron-phonon coupling associated with these transitions. Resistance measurements present nonlinear behavior over similar pressure ranges shedding light on the electronic origin of these pressure-driven isostructural transitions. These multiple indirect signatures of an electronic transition at ~2 GPa and ~4 GPa are discussed in connection with the recent theoretical proposal for $1T$-$TiTe_2$ and also the possibility of an electronic topological transition from our electronic Fermi surface calculations. Between 4 GPa and ~8 GPa, the c/a ratio shows a plateau suggesting a transformation from an anisotropic 2D layer to a quasi-3D crystal network. First-principles calculations suggest that the 2D to quasi-3D evolution without any structural phase transitions is mainly due to the increased interlayer Te-Te interactions (bridging) via the charge density overlap. In addition, we observed a first-order structural phase transition from the trigonal ($P\bar{3}m1$) to monoclinic ($C2/m$) phase at higher pressure regions. We estimate the start of this structural phase transition to be ~8 GPa and also the coexistence of two phases [trigonal ($P\bar{3}m1$) and monoclinic ($C2/m$)] was observed from ~8 GPa to ~16 GPa.

DOI: 10.1103/PhysRevB.97.085107

I. INTRODUCTION

Recently a new state of quantum matter known as topological insulators (TIs) has received a great deal of attention due to their potential applications in spintronics, quantum computing, and thermoelectric energy conversion devices [1]. TIs are a novel class of materials which are insulating in their bulk but support spin-dependent and time reversal symmetry protected conducting states at the boundaries due to strong spin-orbit coupling (SOC) [1,2]. Interestingly, some SOC narrow band gap materials are trivial insulators at ambient conditions but can be transformed into nontrivial topological insulators by applying strain. This transition is named the topological quantum phase transition (TQPT) [3–5]. It is an isostructural second-order transition which arises as a consequence of an adiabatic band inversion occurring at the time reversal invariant momenta point (TRIM) with parity change (odd/even). In this process, the topological invariant Z_2 changes from $Z_2 = 0$ (conventional insulator) to $Z_2 = 1$ (topological insulator) [1,3–5]. Generally, strain can be induced into the SOC materials by either chemical or physical routes. For instance, chemical doping in $TiBi(S_{1-x}Se_x)_2$ [6,7] and $Pb_{1-x}Sn_xSe$ systems [8] causes TQPT. Similarly, the experimentally accessible physical strain, i.e., hydrostatic pressure, is another ideal external tool to tune the SOC strengths, hybridization, density, and crystal field splitting in narrow band gap materials which may induce TQPT. Indeed hydrostatic pressure induced TQPT has been observed in several systems such as BiTeI, BiTeBr, and Sb_2Se_3 [9–11].

Due to its technological importance, a considerable number of materials have been theoretically predicted as a topological insulator under high pressure. However, a direct experimental detection of band inversion with the high-pressure setup is challenging to perform. For example, angle-resolved photoemission spectroscopy (ARPES) is the most direct tool to probe the nontrivial electronic band inversion [12,13]. But ARPES measurements under pressure have not yet been implemented due to the experimental difficulties. However the indirect evidence of TQPT can be obtained from a combination of transport, synchrotron x-ray diffraction (XRD), and Raman linewidth anomalies [9–11,14,15]. Electron-phonon coupling is the basic mechanism for detecting the indirect signatures of TQPT (or band inversion) through optical phonons via Raman spectroscopy. Mathematically, Raman linewidth is directly proportional to the square of the energy-resolved electron-phonon matrix elements [16], and hence the dynamics of electron-phonon coupling will be strongly replicated at full width at half maximum (FWHM) [11,14]. Especially for a centrosymmetric space group, long-wavelength optical phonons

*Corresponding author: cbhas@jncasr.ac.in

($q = 0$) couple to electrons either through commutation or anticommutation with an electronic parity operator and hence effectively capture the changes in topological invariants via linewidth [16]. Though an axial (c/a) ratio as a function of pressure is expected to give the relative compressibility (isotropic or anisotropic), fluctuations in an electronic density due to band inversion cause anomalies in it (c/a ratio) [9,10].

For instance, combined synchrotron powder XRD and infrared spectroscopy measurements on BiTeI [space group (SG) $P3m1$, band gap $E_g = 0.38$ eV] revealed a correlation between band gap closing and band inversion with a minimum of c/a ratio in the pressure range 2.0–2.9 GPa [9,17]. Interestingly, a phonon linewidth anomaly (unusual electron phonon coupling) of the E mode at ∼3.0 GPa has been observed during TQPT in BiTeI [14]. Furthermore, an unusual increase in the inner Fermi surface shape and curvature changes of the outer Fermi surface shape have been noticed from Shubnikov–de Haas oscillations measurements during the TQPT in BiTeI [18]. Similarly, TQPT has been claimed in Sb_2Se_3 (SG *Pnma*, $E_g = 1$ eV) at ∼2.5 GPa by studying the vibrational phonon and electrical resistivity anomalies together with first-principles calculations [11,15], though there is also an alternate interpretation suggested [19]. Recently, Ohmura *et al.* showed that bismuth tellurihalide BiTeBr (SG $P3m1$, $E_g = 0.55$ eV) undergoes a TQPT at 2.5–3.0 GPa using resistivity and synchrotron XRD measurements under pressure [10]. The above examples provide the strong basis for using such indirect methods (XRD and Raman scattering) to study pressure-induced TQPT in SOC systems and provide relevant information.

Titanium-based transition-metal dichalcogenides (TMDs) TiX_2 (X = Te, Se, and S) crystallize in layered hexagonal structure (SG $P\bar{3}m1$, No. 164) which shows exotic properties such as charge density waves and superconductivity [20,21]. Among these $TiTe_2$ has recently received significant interest due to its series of topological transitions under moderate pressures and potential usage for information processing [22,23]. The unit cell of $1T$-$TiTe_2$ consists of stacks of hexagonal close packed layers of Ti metal atoms sandwiched between two adjacent layers of Te atoms and in each layer, the Ti atom is octahedrally surrounded by six Te atoms. It has predominately weak van der Waals type interlayer bonding forces along the c axis and strong intralayer covalent bonds along the ab plane. First-principles calculations based on density functional theory (DFT) predicted a series of pressure-induced transitions between topologically trivial and nontrivial phases related to the band inversions at different points (L, M, and Γ) of the Brillouin zone in $TiTe_2$ [23]. This remarkable theoretical prediction strongly motivated us to explore the pressure-induced topological changes in $TiTe_2$ compounds through XRD, Raman scattering, and electrical transport measurements. To the best of our knowledge, to date, there have been no experimental studies reported on $1T$-$TiTe_2$ under pressure.

In this paper, we present the structural, vibrational, and electrical transport properties of $1T$-$TiTe_2$ under hydrostatic compression. The synchrotron XRD, Raman scattering, and electrical transport anomalies show signatures of the two isostructural electronic transitions at ∼2 GPa and ∼4 GPa in the $1T$ phase, which we have attributed to the nontrivial TQPT and the trivial metallic transition, respectively, based on a recent theoretical report [23]. Further, the applied pressure switches the 2D layered material (anisotropic) to an isotropic 3D crystal above ∼4 GPa through charge density overlapping between the interlayer Te atoms along the c axis. The experimental evidence of isotropic 3D behavior (constant c/a ratio) was explained using first-principles theoretical calculations. This is followed by the $1T$ phase undergoing a pressure-induced structural transition from trigonal (SG $P\bar{3}m1$) to monoclinic (SG $C2/m$) phase at ∼8 GPa. Finally, the theoretically calculated pressure-dependent electronic band structure and Fermi surface show the occurrence of an electronic topological transition (ETT) at 9 GPa (close to the experimental value ∼8 GPa) in the $1T$ phase.

II. EXPERIMENTAL DETAILS

The $1T$ phase of $TiTe_2$ was synthesized by mixing 0.1579 g of titanium shots (99.99%, Alfa Aesar) and 0.8420 g of tellurium shots (99.99%, Alfa Aesar) in a 9 mm diameter quartz tube. The tube was flame-sealed under a vacuum of 10^{-3} Torr, achieved with the help of a rotary pump, to prevent oxidation during heating. The tube was then placed in a vertically aligned tube furnace and heated to 800 °C over a period of 8 h to allow proper homogenization. Subsequently, the temperature was kept constant for 6 days. Finally, the system was allowed to cool to room temperature over a period of 10 h. No reaction with the quartz tube was observed. A black polycrystalline $TiTe_2$ was formed.

Raman spectra were recorded using a WITec micro Raman spectrometer (UHTS600) in the backscattering geometry (180°). The Raman spectrometer was equipped with a diode-pumped frequency-doubled Nd:YAG solid state laser (wavelength $\lambda = 532$ nm), 600 mm focal length monochromator, and Peltier air-cooled CCD detector. The spectral resolution was about ∼0.5 cm^{-1} for a grating of 2400 lines per mm. The *in situ* high-pressure Raman scattering measurements were performed using a membrane-type diamond anvil cell (DAC) with a culet size of 400 μm. A T301 stainless steel gasket with a starting thickness of about ∼250 μm was pre-indented to a thickness of about ∼60 μm. Then a hole of ∼150 μm diameter was drilled at the center which acts as the sample chamber, and the pressure was calculated with the ruby fluorescence method [24]. A mixture of methanol:ethanol (4:1) was used as the pressure-transmitting medium (PTM) which guarantees the hydrostatic limit up to ∼10.5 GPa and quasihydrostatic limit up to 25 GPa [25]. The accumulation time of each spectrum was about 5 minutes. A lower value of laser power (< 0.5 mW) was maintained to avoid the risk of heating and oxidation of the samples.

The *in situ* high-pressure synchrotron XRD experiments were carried out using a Mao-Bell type DAC with diamonds having a culet size of 400 μm. The synchrotron radiation XRD measurements were performed at the Xpress beamline of Elettra, Trieste, Italy, using monochromatic radiation with energy of $E = 24.762$ keV ($\lambda = 0.50070$ Å). The procedures of gasket preparation, PTM, and pressure calibration are the same as mentioned above. The XRD patterns were collected using a MAR345 image plate detector. Typical exposure time was about 4 minutes for each pattern. The calibration of a sample to detector distance and the image plate orientation

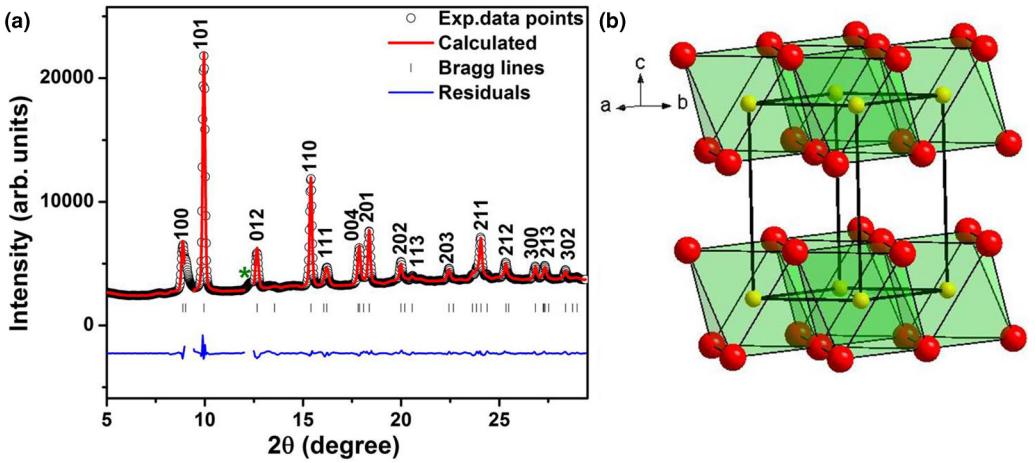

FIG. 1. (a) Rietveld refinement of the synchrotron XRD pattern of $1T$-$TiTe_2$ at ∼0.36 GPa and (b) schematics of the unit cell of $1T$-$TiTe_2$. The yellow and red color atoms represent the Ti and Te, respectively.

angles were carried out using LaB_6 as a standard. The two-dimensional (2D) XRD image patterns were converted into one-dimensional (1D) intensity versus diffraction angle (2θ) patterns using the Fit2D software [26].

Pressure-dependent electrical resistance was measured up to ∼16 GPa at room temperature with the standard quasi-four-probe method using a miniature DAC and an ac-resistance bridge in combination with fine gold electrodes fabricated on the diamond culet. The sample and electrodes were insulated from the metal gasket using an insulation layer of Al_2O_3 and epoxy mixture. The sample pressure was measured with the *in situ* ruby fluorescence method at room temperature [24]. Powdered NaCl was used as the PTM which not only maintains quasihydrostaticity but is also used to keep the electrodes in good contact with the sample.

III. COMPUTATIONAL METHOD

The calculations were carried out within the frame work of DFT implemented in the CASTEP and WIEN2k packages [27,28]. The experimental parameters are considered as an input, and the structure was optimized using the Broyden-Fletcher-Goldfarb-Shanno (BFGS) minimization scheme [29]. The optimized structure was used to calculate the bonding and electronic structure properties, which was performed using the WIEN2k package with the generalized gradient approximation of Perdew, Burke, and Ernzerhof (GGA-PBE) functional [30]. Considering the presence of heavy elements we have included spin-orbit coupling in the calculations. A dense k mesh of $39 \times 39 \times 19$ was used and all the calculations were performed with the optimized lattice parameters with an energy convergence criterion of 10^{-6} Ry per formula unit. Raman spectra were calculated with the CASTEP package.

IV. RESULTS

A. Characterization of $TiTe_2$ at ambient conditions

The Rietveld refinement of the XRD pattern for the $P\bar{3}m1$ structure (referred to as the $1T$ phase) is shown in Fig. 1(a). The calculated cell parameters and volume at ∼0.36 GPa are $a = 3.76416$ Å, $c = 6.46711$ Å, and $V = 79.355$ Å^3, respectively, which show good agreement with the $1T$ phase of the previous report at ambient conditions [31,32]. The typical unit cell for the $1T$ structure is shown in Fig. 1(b). There are three atoms in the unit cell of $1T$-$TiTe_2$, where Ti^{4+} and Te^{2-} atoms occupy 1a and 2d Wyckoff sites, respectively. Further, the presence of a small elemental Te has been detected in the synchrotron pattern and is indicated by green color asterisk symbols in Fig. 1(a). We have carefully excluded the Te regions during the refinements.

According to group-theoretical analysis, the layered $1T$ structure of $TiTe_2$ has nine vibrational modes at the gamma point of the phonon dispersion curve [33,34]:

$$\Gamma = E_g + A_{1g} + 2E_u + 2A_{2u},$$

where the gerade (E_g and A_{1g}) and ungerade (E_u and A_{2u}) modes represent the Raman-active and IR-active phonon modes, respectively. In this centrosymmetric structure, the doubly degenerate E_g mode (symmetric in-plane bending) represents the atomic vibrations along the ab plane whereas the A_{1g} mode (symmetric out-of-plane stretching) represents the atomic vibrations parallel to the c axis as shown in Fig. 2.

Raman modes were fitted using the Lorentzian line shape function. Based on our theoretical calculation and the existing literature, the phonon modes at ∼105 cm^{-1} and ∼143 cm^{-1} are assigned to E_g and A_{1g} symmetry, respectively [33–35]. However, we observed an additional strong mode at ∼126 cm^{-1}, named the M mode. This mode was seen in a few layers of $TiTe_2$ grown as a thin film by Khan *et al.* and was attributed to E_g symmetry [22]. This assignment seems to be unreliable since a polarization-dependent study on single crystals confirmed that the selection rule allowed two Raman-active modes (E_g and A_{1g}) and its energies are ∼102 cm^{-1} and ∼145 cm^{-1}, respectively [35]. Recent accurately calculated vibrational modes of $TiTe_2$ closely match with our assignment [33]. Hence this M mode could be a zone-folded Raman-active mode and has been observed in prototype $1T$ phase layered TMD materials at different conditions [36–38]. However, the polarization and temperature dependent behavior of this mode (M) in the few layers may give more insight into this mode, which is the subject of future interest. The detailed comparative

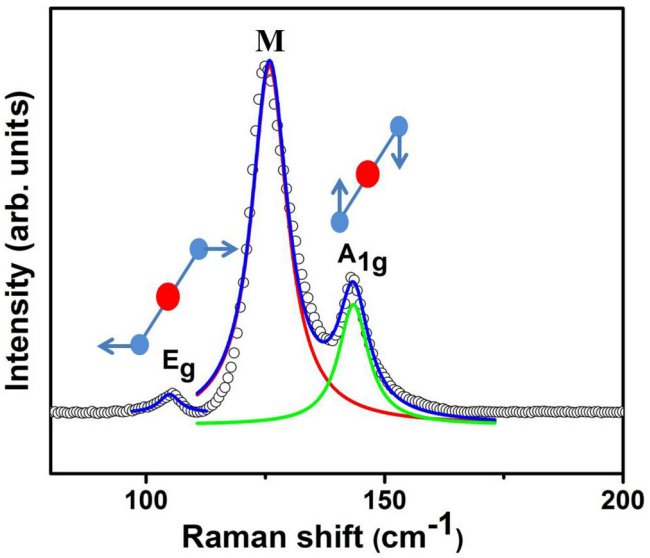

FIG. 2. Raman spectrum of $1T$-$TiTe_2$ at ambient conditions.

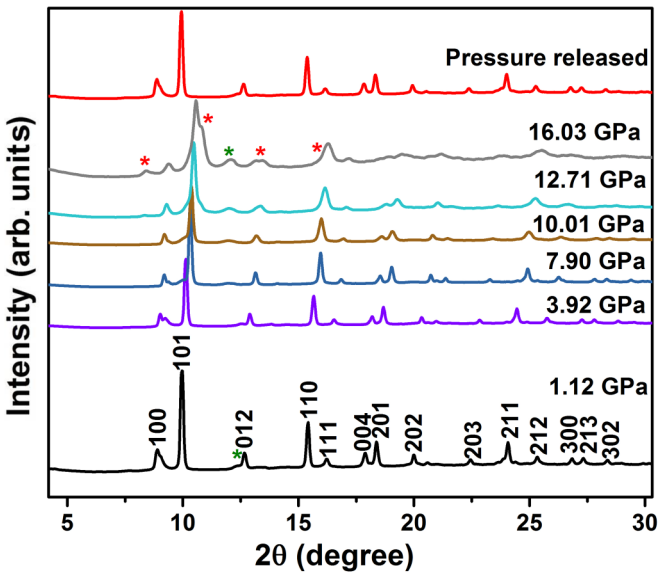

FIG. 3. Pressure evolution of the synchrotron XRD patterns of $TiTe_2$ at selected pressure values. The red color asterisk symbol represents the appearance of new Bragg peaks at higher pressure regions.

analysis of vibrational energies for the $1T$-$TiTe_2$ compound is shown in Table I.

B. Synchrotron XRD measurements under pressure

In situ high-pressure synchrotron XRD measurements were carried out up to ∼16 GPa and the representative XRD plots for selected pressures are shown in Fig. 3. The systematic increase in the Bragg peaks to higher diffraction angle (2θ) is consistent with the compression of the unit cell. Furthermore, the appearances of new Bragg peaks at ∼12.0 GPa indicate structural transition. However, the onset of the phase transition point can be traced to ∼8 GPa via the (101) and (110) Bragg peak analysis (by peak fitting) and this has been commented on in the Supplemental Material [Figs. S1(a) and S1(b)] [39]. By comparing our XRD patterns (Fig. 3) with prototype compounds such as $IrTe_2$ and ZrS_2 (CdI_2 type structure), we found that $TiTe_2$ follows an identical structural sequence to $IrTe_2$ and ZrS_2 under high pressure [40,41]. Notably, a distinct splitting of the (101) Bragg peak observed in $TiTe_2$ is exactly in agreement with $IrTe_2$ and ZrS_2 [40,41]. Even though a new high-pressure phase appears in $TiTe_2$, the ambient phase coexists up to ∼16.0 GPa, the maximum pressure reached in this study. The structural evolution of the Te phase (shown as the green asterisk in Fig. 3) under pressure is well established; hence a discussion on the high-pressure phases of Te was excluded in the whole pressure range of this study.

In the $1T$ phase, the only free atomic position is the z coordinate of the Te ions which defines the Te(1)-Te(2) contact distance. The lattice parameters and atomic coordinates are refined using the FullProf software [42] for each XRD pattern up to 8 GPa. After ∼8 GPa, due to the complexity of the mixed phases, we analyzed the $1T$ phase of $TiTe_2$ using Powd and Dicvol software [43], which provides only the unit cell parameters (a, b, c) and volume (V). Figure 4 represents the systematic decrease in volume of the unit cell up to ∼16 GPa. Notably, an apparent change is observed at ∼8 GPa, which further ascertains the phase transition. The pressure-volume data best fitted the equation of state (EOS) into two different regions using the following Murnaghan EOS and third-order Birch-Murnaghan EOS, respectively [44,45]:

$$P(V) = \frac{B_0}{B_0'}\left[\left(\frac{V_0}{V}\right)^{B_0'} - 1\right],$$

$$P(V) = \frac{3B_0}{2}\left[\left(\frac{V_0}{V}\right)^{\frac{7}{3}} - \left(\frac{V_0}{V}\right)^{\frac{5}{3}}\right] \times \left\{1 + \frac{3}{4}(B_0' - 4)\left[\left(\frac{V_0}{V}\right)^{\frac{2}{3}} - 1\right]\right\},$$

TABLE I. The assignment of the Raman modes for $1T$-$TiTe_2$.

	Experimental frequency (cm^{-1})			Theoretical frequency (cm^{-1})		
Raman mode	This work	Ref. [35][a]	Ref. [22][b]	This work	Ref. [34]	Ref. [33]
E_g	105	102		100	105	99.1
M	126		124			
A_{1g}	143	145	145	140	150	145.1

[a]Single crystal.
[b]Few layers.

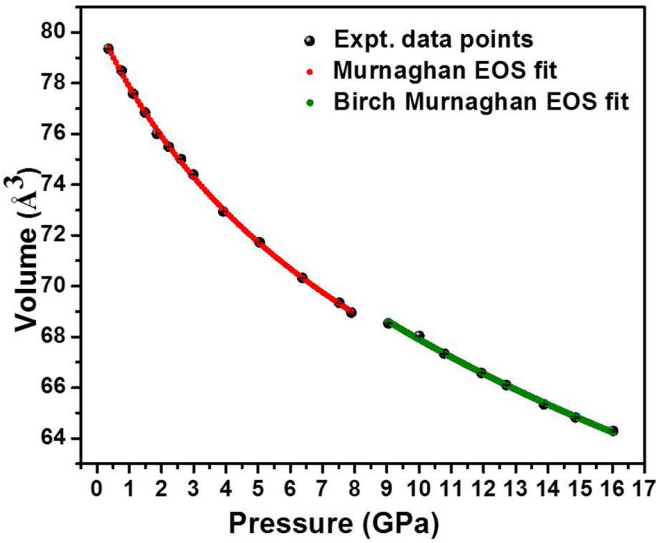

FIG. 4. EOS fit for the $1T$-$TiTe_2$ phase to the pressure versus volume data.

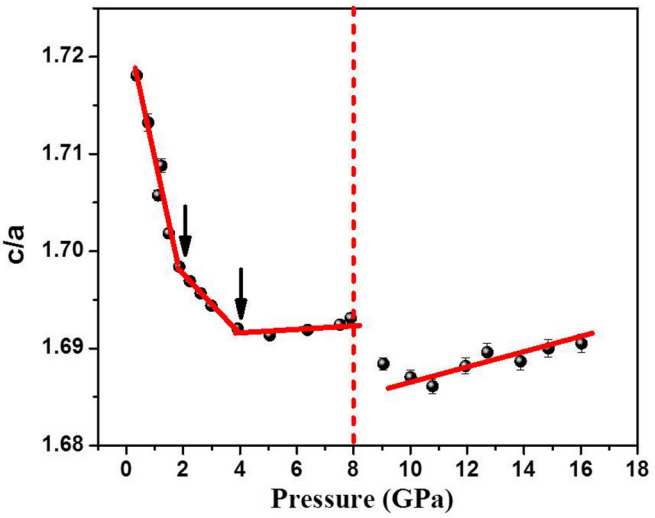

FIG. 5. Pressure dependence of the c/a ratio for $1T$-$TiTe_2$. The solid and vertical dotted lines signify a guide to the eye and structural phase transition, respectively.

where B_0, B_0', and V_0 are the isothermal bulk modulus, the derivative of the bulk modulus, and the volume at room pressure, respectively. The Murnaghan EOS was used to fit the pressure region up to ~8 GPa and the fit yields $V_0 = 80.34$ Å^3, bulk modulus $B_0 = 28.60$ GPa, and $B_0' = 7.19$. In the mixed phase regions (8–16 GPa), the $1T$ phase was fitted with the third-order Birch-Murnaghan EOS, and the fit gives $V_0 = 79.26$ Å^3, bulk modulus $B_0 = 40.73$ GPa, and $B_0' = 6.02$. After the phase transition, B_0 increases from 28.60 GPa to 40.73 GPa suggesting that the high-pressure $1T$ phase has lesser compressibility than ambient conditions.

The pressure dependence of the normalized lattice parameters (a/a_0, c/c_0) is plotted in Fig. S2 [39]. Though a/a_0 and c/c_0 decrease systematically under pressure up to ~16 GPa, a clear anomaly in a/a_0 at ~8 GPa is observed (see Supplemental Material [39]). Figure 5 represents the pressure versus c/a ratio of $1T$-$TiTe_2$. Initially, the c/a ratio decreases from 1.718 to 1.690, implying that the c axis is more compressible than the a axis which is usually expected for anisotropic layered crystals due to the weak van der Waals interlayer forces along the c direction. Interestingly, two inflection points are noticed in the $1T$ phase at ~2 GPa and ~4 GPa. Here, we would like to emphasize that a similar trend was reported in the pressure ranges 2.0–2.9 GPa and 2.5–3.0 GPa in BiTeI and BiTeBr, respectively, and these changes were interpreted as the signature of TQPT [9,10]. To get more insight about c/a ratio anomalies, the pressure-dependent Te(1)-Te(2) contact distance is plotted in Fig. S3 [39]. As seen from Fig. S3, it shows two distinct anomalies in the $1T$ phase region at ~2 GPa and ~4 GPa. But after 4 GPa, the c/a ratio surprisingly turns out to be almost pressure invariant which suggests that the compressibilities of both the lattice parameters (a and c) are similar. A plausible cause for this behavior could be because the lower threshold level of the Te(1)-Te(2) anionic contact distance is reached and strong charge repulsion (Coulomb) is built up between the interlayers. Hence this constant behavior of the c/a ratio under pressure hints at the isotropic nature. So, the pressure switches the 2D layered $1T$-$TiTe_2$ into a quasi-3D network like feature from 4 GPa to 8 GPa, and a similar observation has been made in $MoSe_2$ [46]. This change in axial compressibility is directly related to the fluctuations in the charge density distribution along the different directions, as we discuss in more detail below (theoretical results). In the pressure region 4–8 GPa, a huge amount of strain is developed inside the sample. In order to relax the strain, the $1T$ phase undergoes a structural phase transition. Evidently, the discontinuity in c/a ratio at ~8 GPa indicates the structural transition and further it increases with pressure. Therefore, in the $1T$ phase, initially the a axis is stiffer than the c axis, and after the structural transition, the c axis is stiffer than the a axis.

$IrTe_2$ also undergoes a pressure-induced structural transformation from $P\bar{3}m1$ to $C2/m$ at ~5 GPa [40]. Due to the poor data quality and complexity of the mixed phase, we could not refine this phase through the Rietveld method from ~8 GPa onwards. However, we have indexed the XRD pattern at ~13.90 GPa with the monoclinic $C2/m$ space group using the Powd and Dicvol software [43] as shown in Fig. S4 [39]. The indexed values for the monoclinic unit cell at ~13.90 GPa are $a = 17.3666$ Å, $b = 3.5545$ Å, $c = 5.6966$ Å, $\beta = 91.17°$, $V = 351.57$ Å^3, $Z = 6$, and $V/Z = 58.60$ Å^3, which agree well with the similar prototype system, $IrTe_2$ [40]. The volume change of ~9.5% (when we extrapolate the volume data of the high-pressure phase to ~8 GPa) is observed during the structural transition which confirms the first-order nature of the transition (see Fig. S5) [39]. Mention must be made of the V/Z values of the monoclinic phase ($C2/m$), which very well agree with the V/Z trend of $P\bar{3}m1$ phase as shown in Fig. S5 [39]. During the indexing of the monoclinic $C2/m$ phase, the b axis is considered as the unique axis, and the lattice parameters of the indexed pattern for three different pressure values are given in Table SI (see Supplemental Material [39]). Upon releasing pressure, the high-pressure phase is transformed back to the ambient $1T$ phase indicating reversibility of the transition.

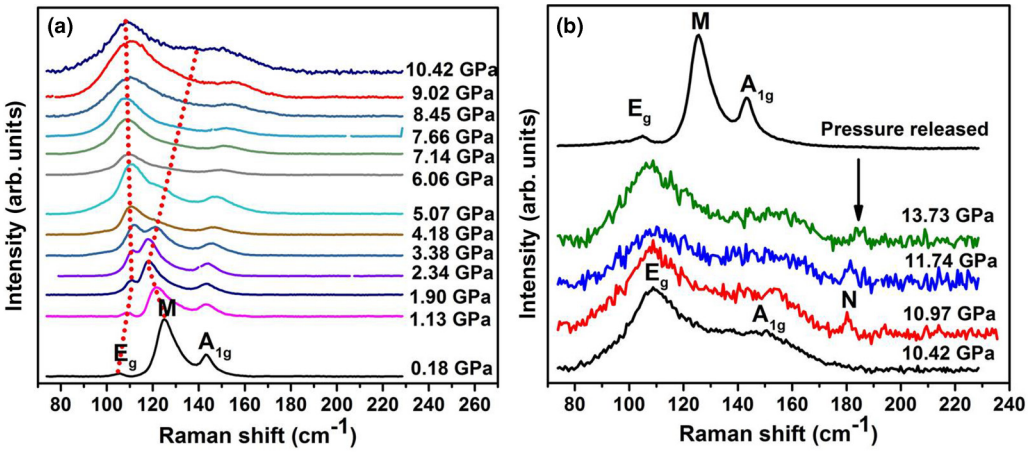

FIG. 6. (a) The representative Raman spectra of $TiTe_2$ at relatively low pressure regions and (b) at high-pressure regions and depressurized ambient Raman spectrum.

The study of detailed pressure-induced structural changes with atomic coordinates is beyond the scope of the present work and will be the future interest of our group.

C. Raman scattering measurements under pressure

To shed light on the observed isostructural anomalies (c/a ratio) and phase transitions in $TiTe_2$, Raman spectroscopy measurement under pressure was employed up to ~13.7 GPa. The pressure evolutions of Raman spectra of $TiTe_2$ are shown in Figs. 6(a) and 6(b). As the pressure increases, the intensity of the E_g mode increases, whereas the intensity of the M and A_{1g} modes are decreasing. However, the overall intensity of all the phonon modes is observed to be drastically decreased above ~8.0 GPa. As evident from Fig. 6(b), the appearance of a new Raman mode at ~10.97 GPa (named the N mode) confirms the structural phase transition and the presence of the E_g and A_{1g} modes at higher pressures confirms the phase coexistence (mixed phase), which is consistent with the XRD results. After ~13.7 GPa, the peaks become very broad and difficult to deconvolute from the background. During the depressurization, the system came back to initial phase ($1T$-$TiTe_2$), which suggests the observed transition is reversible.

The pressure-dependent Raman shift of the E_g, A_{1g}, M, and N modes is shown in Fig. 7(a). In general, the phonon modes are expected to harden (blueshift) during the hydrostatic lattice compression. But, Fig. 7(a) shows that the behaviors of all the modes are anomalous and we can identify four distinct pressure regions. To elucidate this we have fitted in each region A_{1g} and E_g modes using linear equations, and the fitting parameters [slope a_1 and intercept $\omega(P_0)$] are summarized in Table II. The A_{1g} mode softens slightly up to ~2 GPa and thereafter it starts to harden up to ~8 GPa with a small change in slope at ~4 GPa, while the E_g mode shows hardening up to 4 GPa with a clear change in slope at ~2 GPa followed by softening till 8 GPa. Upon further compression, the frequency of the E_g mode and the newly appeared N mode starts to increase, while the A_{1g} mode begins to soften up to ~14 GPa, which is the maximum pressure achieved in Raman study. The frequency of the zone-folded Raman mode M exhibits very interesting high-pressure behavior. It shows two parabolic pressure dependencies with two distinct

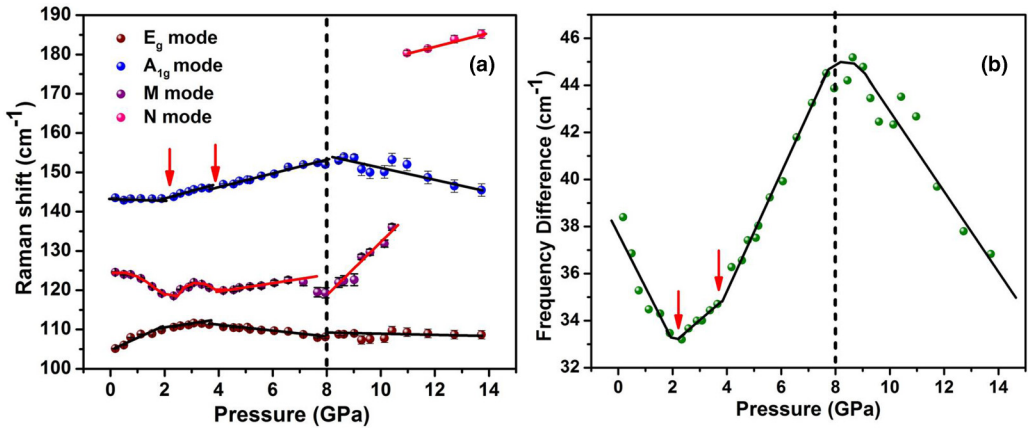

FIG. 7. (a) Pressure versus Raman shift of phonon modes (A_{1g}, M, E_g, and N) of $TiTe_2$. The solid black line represents the linear fit, and the red line represents a guide to the eye. (b) Pressure versus frequency difference ($A_{1g} - E_g$) between the A_{1g} and E_g modes of $TiTe_2$. The solid red arrows at ~2 GPa and ~4 GPa represent the isostructural electronic transitions. The solid and vertical dotted lines represent a guide to the eye and structural phase transition, respectively.

TABLE II. Pressure dependence behavior of various Raman-mode frequencies and Gruneisen parameters (γ) of $1T$-$TiTe_2$. The pressure coefficients for $1T$-$TiTe_2$ were fitted [47] using $\omega(P) = \omega(P_0) + a_1(P - P_0)$. The Gruneisen parameters γ are determined by using the relation $\gamma = \frac{B}{\omega(P0)} \frac{\partial \omega}{\partial P}$, where B represents the bulk modulus.

Raman Mode	$\omega(P_0)$ (cm^{-1})	a_1 ($cm^{-1}GPa^{-1}$)	γ
E_g	105.1 ± 0.6[a]	3.07 ± 0.67[a]	0.84
	109.3 ± 0.7[b]	0.65 ± 0.24[b]	0.17
	113.6 ± 0.4[c]	−0.68 ± 0.07[c]	−0.17
	106.5 ± 2.2[d]	0.20 ± 0.02[d]	0.08
A_{1g}	143.4 ± 0.1[a]	−0.10 ± 0.01[a]	−0.03
	140.2 ± 0.6[b]	1.69 ± 0.20[b]	0.34
	139.5 ± 0.6[c]	1.70 ± 0.10[c]	0.35
	165.9 ± 2.9[d]	−1.46 ± 0.27[d]	−0.36

[a]Estimated at room pressure ($P_0 = 1$ atm).
[b]Estimated at $P_0 = 1.89$ GPa.
[c]Estimated at $P_0 = 4.1$ GPa.
[d]Estimated at $P_0 = 7.95$ GPa.

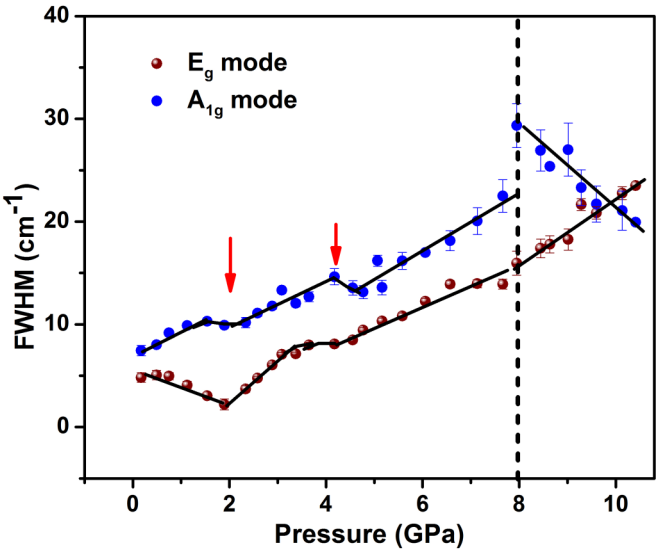

FIG. 8. Pressure dependence of FWHM of A_{1g} and E_g modes for $TiTe_2$. The solid red arrows at ∼2 GPa, and ∼4 GPa indicate the isostructural electronic transitions. The solid and vertical dotted lines represent a guide to the eye and structural phase transition, respectively.

points of inflection at ∼2 and ∼4 GPa, beyond which it slowly hardens up to ∼8 GPa. After the phase transition, the M mode shows significant hardening with pressure. Notably, over the pressure range between 0–2 GPa and also between 4–8 GPa, the pressure dependencies of the A_{1g} and E_g modes show opposite behaviors.

The drastic softening of the E_g mode ($a_1 = -0.68\,cm^{-1}/GPa$) and hardening of the M mode from ∼4 GPa to ∼8 GPa hint at the structural instability and plausible reason for the impending structural phase transition. The slope change of the A_{1g} and E_g modes at ∼8.0 GPa is attributed to the onset of structural phase transition from trigonal ($P\bar{3}m1$) to monoclinic ($C2/m$). The intensity and linewidth of the N mode is smaller compared to that of the A_{1g} and E_g modes. This could be the reason we did not observe the appearance of the N mode at the onset pressure (∼8 GPa) of the structural transition. However, once its intensity evolves under pressure, it comes out above 10.97 GPa. To get more insight, the frequency difference between the A_{1g} and E_g modes is plotted as a function of pressure and represented in Fig. 7(b). The plot illustrates four different regions, which substantiate the analysis of the pressure dependence of the A_{1g} and E_g modes. The maximum in frequency difference ($A_{1g} - E_g$) at ∼8 GPa represents the structural phase transition, whereas the two minima at ∼2 GPa and ∼4 GPa signify the isostructural anomalies.

Raman linewidth studies could provide information about the phonon-phonon interactions and the excitation-phonon interactions such as electron-phonon and spin-phonon coupling existing in the system [47–51]. Therefore, we have carefully analyzed the FWHMs of the A_{1g} and E_g modes and these are shown in Fig. 8. It should be noted that the nature of PTM limits the accuracy of information about intrinsic linewidth of the sample beyond the hydrostatic limit. Since the methanol:ethanol (4:1) mixture gives only the hydrostatic pressure limit up to ∼10.5 GPa, the linewidth of the phonon modes has been analyzed below 10.5 GPa [25]. Generally, for the crystal, Raman linewidth is inversely proportional to the lifetime of the phonon modes. It is normally seen that as we increase the pressure, there is an increase in linewidth of phonon modes. However, the FWHM of the E_g mode decreases under pressure up to ∼2 GPa, followed by an increase up to ∼10.5 GPa with anomalous behaviors at ∼4 GPa and ∼8 GPa. It is noteworthy that a similar pressure-induced decrease in linewidth of the E and E_g modes was observed in BiTeI and A_2B_3 (A = Bi, Sb and B = Te, Se, and S) series compounds during the TQPT at 3–4 GPa and ETT at 3–4 GPa, respectively [14,47,51]. In contrast, the A_{1g} linewidth increases up to 8 GPa with significant anomalies at ∼2 GPa and ∼4 GPa, followed by a decrease up to 10.5 GPa with a discontinuity observed during the phase transition at ∼8.0 GPa. After the structural transition, the decreasing trend in linewidth of the A_{1g} phonon mode could be due to decrease of electron-phonon coupling in the monoclinic $C2/m$ phase. The zone-folded Raman mode M shows increasing linewidth behavior under pressure up to ∼11 GPa, which is the expected behavior for any phonon (see Fig. S6) [39]. More importantly, evidence of an unusual electron-phonon coupling from the linewidth anomalies (A_{1g} and E_g) at ∼2 GPa and ∼4 GPa further confirms the isostructural ($P\bar{3}m1$) transitions, which could possibly be originated from electronic state modulation under pressure. Finally, the pressure-dependent frequency and linewidth behavior of both the A_{1g} and E_g modes suggests two isostructural transitions and a structural transition, which is quite consistent with the XRD measurement.

D. Electrical transport measurements under pressure

$1T$-$TiTe_2$ is expected to show metallic behavior due to the finite band overlap of the d orbitals of the Ti atom with the p orbitals of the Te atoms at ambient conditions [52]. The oxidation state of typical CdI_2 structures such as TiX_2

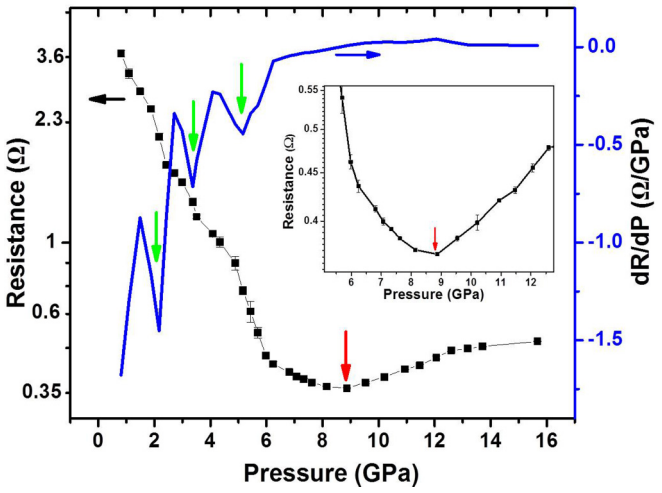

FIG. 9. Pressure-dependent electrical resistance of $TiTe_2$ (black square and a line corresponding to the left y axis) and its first derivative (blue line corresponding to the right y axis). The red arrow at ∼8.8 GPa indicates the structural transition. The solid green arrows at 2.1 GPa and 3.4 GPa indicate the isostructural electronic transitions in the trigonal ($P\bar{3}m1$) phase. The inset highlights the resistance minimum in the vicinity of the structural transition.

is given by $Ti^{4+}(X^{2-})_2$ (X = S, Se, and Te); here the amount of electron transfer from orbitals p to d is zero [53]. However the overlap of the p orbitals with the d orbitals can lead to the transfer of n electrons per metal; then the oxidation formula can be changed into $Ti^{(4-n)+}(X^{[2-(n/2)]-})_2$ [53]. In the energy band diagram, the transition-metal Ti-d orbitals are located just above the top of the p orbitals of Te chalcogen [53]. These two orbitals can be overlapped either via the chemical or physical methods. Chemically, it can be achieved by decreasing the electronegativity of chalcogen X. As the electronegativity of Te is less than both Se and S, the top portions of the p orbital bands are raised. Hence, the overlap of p-d bands is more in Te than in Se and S atoms which leads to the behavior of $TiTe_2$, $TiSe_2$, and TiS_2 as metal, semimetal, and semiconductor, respectively. Physically, the overlap of the p-d orbitals can be increased by reducing the Ti-X bond distance, which can be experimentally achieved using hydrostatic pressure.

In this paper, we have investigated the pressure-dependent resistance measurements of a polycrystalline $1T$-$TiTe_2$ sample at room temperature. The pressure dependence of the electrical resistance (R) and its first derivative (dR/dP) at room temperature for $1T$-$TiTe_2$ are illustrated in Fig. 9. The resistance value is ∼3.7 Ω for the lowest measured pressure (∼0.8 GPa). For the $1T$-$TiTe_2$ sample (single crystal), Koike *et al.* [54] and de Boer *et al.* [55] reported that the resistivity at room temperature is of the order of 10^{-4} Ω cm (at low temperature it is of the order of 10^{-5} Ω cm). Then the resistance of a sample with a few microns thickness will be of the order of 1 Ω. In our measurements, it is 3.7 Ω at 0.8 GPa. So, its order of magnitude is more or less consistent with the literature [54,55]. Because of the soft polycrystalline nature of the sample (small pressure can change the sample thickness by a huge amount), we have not measured the thickness of the sample at ambient pressure, and the low-pressure resistance measurements have no meaning (in the low-pressure region the intergrain contribution is large compared to the sample contribution). We have measured the resistance above a sufficient pressure ($P > 0.8$ GPa) although at this pressure the intergrain contribution is there, but will definitely be small compared to the sample resistance. Therefore, we believe that the obtained resistance of the polycrystalline $1T$-$TiTe_2$ sample provides a real trend, without being affected by the wire-contact resistance or contribution of the intergrain barriers.

As the pressure increases, the resistance of the $TiTe_2$ sample quickly drops from ∼3.7 Ω at ∼0.8 GPa to ∼0.37 Ω at ∼8.8 GPa. As we further increase the pressure from 8.8 GPa the resistance starts to increase slowly with pressure (clearly seen in the inset of the Fig. 9) and at ∼12.6 GPa reaches a value of ∼0.48 Ω which is 30% more than that at ∼8.8 GPa. Above ∼12.6 GPa the resistance increases at a slower rate and the 0.51 Ω resistance at ∼16 GPa (the highest measured pressure of our experiment) is roughly 38% more than at ∼8.8 GPa. The increase in resistance may be caused by sample size shrinkage. Fritsch *et al.* [56] suggested that the increase in resistance by the sample size shrinkage is about one third of the compressibility, which in the present case should be less than 10% below ∼8.8 GPa and 13% at 16 GPa based on the bulk modulus measurements of our XRD experiment. Thus, our result suggests that as the pressure increases, $TiTe_2$ becomes more and more metallic only up to 8.8 GPa and the unusual increase of the resistance above ∼8.8 GPa should mainly result from the accompanying change in the crystal structure which is consistent with the structural transition from trigonal ($P\bar{3}m1$) to monoclinic ($C2/m$) as confirmed by XRD and Raman measurements at ∼8 GPa. This type of change in crystal symmetry along with abnormal resistance increase with pressure was also observed in V_2O_3 [57]. It is also reported that the pressure-induced structural phase transitions of Bi_2Te_3 and As_2Te_3 induce a series of changes in the electrical resistivity [58,59].

In the low-pressure regime (below 8.8 GPa), the pressure-dependent resistance curve shows three distinct slope changes at ∼2.1 GPa, ∼3.4 GPa, and ∼5.1 GPa which are identified by the minima of the P vs dR/dP curve. These inflection points cannot be associated with structural phase transitions since high-pressure XRD and Raman measurements reveal the structural stability of the ambient-pressure $P\bar{3}m1$ structure up to ∼8 GPa and are associated with isostructural electronic transitions. The first two points (∼2.1 GPa and ∼3.4 GPa) are consistent with our XRD and Raman measurements (∼2 GPa and ∼4 GPa). Here, we would like to mention that anomalies in pressure-dependent transport (resistivity) measurements at room temperature were observed in BiTeBr during the TQPT at 2.1 GPa [10]. The third transition point at ∼5.1 GPa is not seen in XRD and Raman measurement. We have seen from XRD that the strains build up in the pressure range of 4–8 GPa followed by a structural phase transition at ∼8.8 GPa. In addition, we observe the broad nature of the minimum at ∼5.1 GPa of the dR/dP curve. Hence, the anomaly at ∼5.1 GPa may be the signature of the precursor effect for the structural transition. We observe a considerable hysteresis between the pressure-increasing and pressure-decreasing cycle, which confirms the first-order nature of the transition at ∼8.8 GPa (see Fig. S7) [39]. The irreversibility of the resistance upon

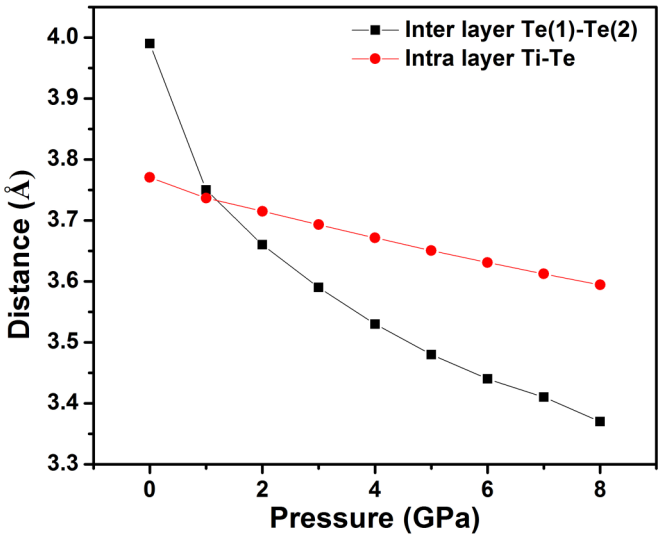

FIG. 10. Pressure dependence of the interlayer Te(1)-Te(2) and intralayer Ti-Te distance.

decompression is noted, and which may happen for various reasons. (i) One of the most important reason is that we might not have given sufficient time for releasing (for example, see supplementary of Ref. [60]). The other reasons are (ii) irreversible changes in the shape and size of the materials upon decompression, and that (iii) the high-pressure structural transition may not be completely reversible. Here the structure is entirely reversible, inferred from the high-pressure XRD and Raman data, and hence this possible reason is ruled out. But, the first two possibilities are not entirely ruled out and could play an important role in the observed irreversibility of the resistance. More importantly, the isostructural and structural transition observed in resistance studies is consistent with multiple techniques such as XRD and Raman measurements over similar pressure regions, which further ascertains that the transitions are intrinsic. The small difference in transition pressure observed with respect to XRD and Raman could be mainly due to the sensitiveness of these techniques, error in pressure measurement, and the degree of hydrostatic conditions produced by PTM used in these experiments.

E. First-principles calculations

The experimental observations in the present work demonstrate a series of transitions at 2 GPa, 4 GPa, and at 8 GPa, wherein the first two transitions were isostructural, while the last one was found to be a first-order structural phase transition. In addition, the system is found to evolve with increased 3D nature from an anisotropic 2D form, which occurs within the pressure range of 4–8 GPa. To have a better understanding of these isostructural transitions, we have performed first-principles electronic structure calculations. We have optimized the ground state, and the optimized parameters are in good agreement with those of the present work. We first intend to investigate the quasi-3D nature of $1T$-$TiTe_2$ via charge density redistribution.

Here, we have analyzed the interlayer Te(1)-Te(2) bonding, intralayer Ti-Te bonding, and charge density plots. Bond lengths of both interlayer Te(1)-Te(2) and intralayer Ti-Te are plotted as a function of pressure as shown in Fig. 10. Due to the layered nature, the interlayer Te(1)-Te(2) bond length is higher than the intralayer Te-Ti bond length at ambient conditions. Under the application of pressure above 2 GPa the intralayer Ti-Te bond length is more than the interlayer Te-Te bonding, which might result in the reduction of 2D character and increased overlap of orbitals between p and d.

Likewise, the bond length between Te(1) and Te(2) decreases with compression, which will increase the charge flow between these two layers and is clearly seen in charge density plots (Fig. 11). Figures 11(a) and 11(b) represent the charge density plots [(111) plane] both at ambient and 8 GPa, respectively (for other pressure values, see Fig. S8 [39]). At ambient, we observed a more ionic nature between the interlayer Te(1) and Te(2). With pressure, this ionic nature is found to decrease, and the covalent nature is found to increase. In Fig. 11, we have shown the intralayer Ti-Te bonding as a function of pressure and we observe a large overlap between intralayer Ti-Te, which will cause more charge flow between them. In addition to this, the layer thickness is found to decrease with pressure, and the Te-Ti-Te angle is found to increase with pressure.

We have systematically analyzed the band structure and Fermi surface of $1T$-$TiTe_2$ in more detail for each pressure. The calculated band structure and Fermi surface at ambient and

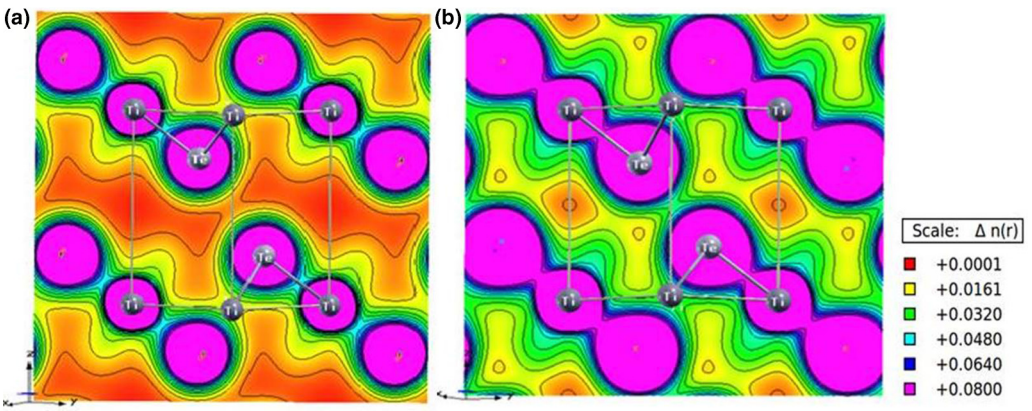

FIG. 11. (a) Pressure-dependent charge density redistribution of (111) plane at 0 GPa and (b) 8 GPa. The relative scale of the charge density is given in the color code.

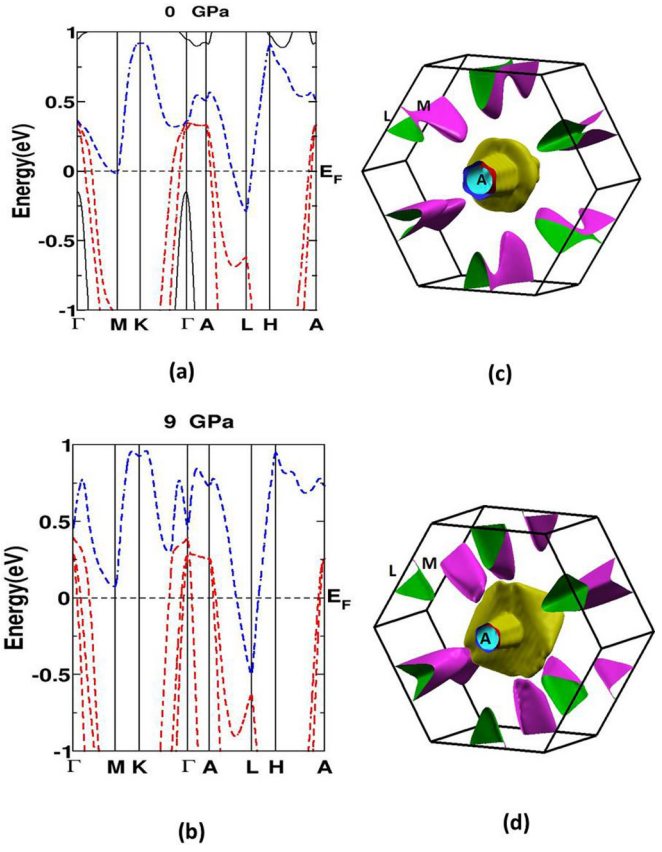

FIG. 12. (a), (b) Band structure and (c), (d) Fermi surface of $1T$-$TiTe_2$ at ambient and 9 GPa. Hole-like bands are given in red color and electron-like bands are given in blue color.

9 GPa are given in Fig. 12 and the rest of the pressure ranges are given in Fig. S9 [39]. From the figures, it is quite evident that the nature of the band structure changes as a function of pressure at small pressure itself (see Fig. S9 for 2 GPa [39]). Since the band nature is changing little far from the Fermi level, the Fermi surface plots do not show a significant difference at 2 GPa. Still, we can see the extent of overlap increasing along M-L as a function of pressure. A similar scenario is observed in the case of 4 GPa. Detailed analysis at higher pressure (at 9 GPa) reveals a change in band nature near the Fermi level which causes corresponding changes in Fermi surface, as seen in Fig. 12(d). At ambient, three bands are crossing the Fermi level, of which two are hole-like pockets and one is an electron-like pocket. From 2 GPa onwards one can see an additional hole-like pocket added to it. The fourth band (electron-like pocket) which crosses the Fermi level along the M to L high-symmetry direction produces a connected Fermi surface at lower pressure range. In the case of the high-pressure state, the fourth band alignment got lifted up at the M point, and it crosses the Fermi level only around the L point, which is clearly seen from the Fermi surface. The changes in the band topology of electronic Fermi surfaces are called ETT or the Lifshitz transition [61]. Here, the overall band and Fermi surface topology changes are observed around 9 GPa, which is very close to the experimental value of 8 GPa suggesting an ETT. In addition to that nonmonotonic variation of the density

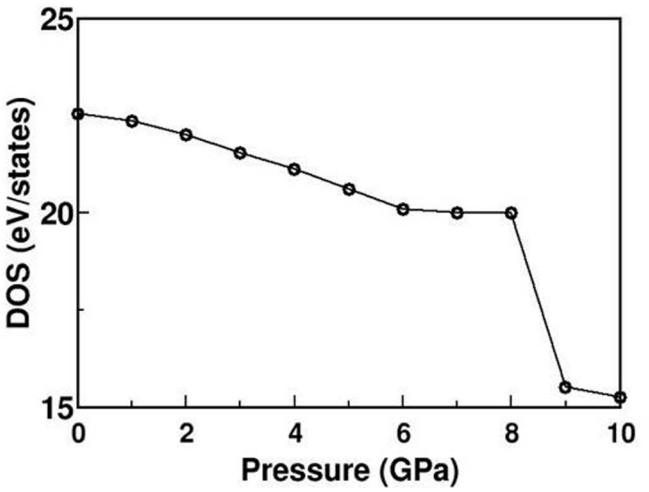

FIG. 13. Variation of the DOS at Fermi level for $1T$-$TiTe_2$ as a function of pressure.

of states (DOS) [62] at the Fermi level supports the presence of ETT around 9 GPa, and the same is given in Fig. 13.

V. DISCUSSION

The recent theoretical calculation showed that $1T$-$TiTe_2$ undergoes a series of topological transitions under hydrostatic isothermal compression [23]. $1T$-$TiTe_2$ is shown to have four consecutive band inversions at the A, L, Γ, and A points corresponding to the theoretical pressure points of 0.88 GPa, 3.40 GPa, 10.7 GPa, and ∼26.4 GPa, respectively [23]. The transition pressure values are calculated from the comparisons of the experimental EOS with the theoretically predicted value [23] and details are mentioned in the Supplemental Material [39]. Due to the first band inversions at the A point (∼0.88 GPa), the system possesses nontrivial TQPT due to the changes in the parity and consequently the topological invariant changed to $Z_2 = 1$. This is followed by another band inversion (∼3.40 GPa), which takes place at the L point of the Brillouin zone. This leads the system to become a trivial metallic phase because the net parity change is the same with respect to the ambient condition ($Z_2 = 0$) [23]. Furthermore, there is another band inversion (∼10.7 GPa) at the Γ point, which changes the overall parity and hence the topological invariant (Z_2) changes from 0 to 1, leading to a second nontrivial TQPT. Finally, the band inversion (∼26.4 GPa) at the A point in the BZ makes the system switch back to the trivial metallic phase ($Z_2 = 0$). Interestingly, it is suggested that if there are no phase transitions this cycle of multiple oscillations of topological transition should continue [23].

The experimentally observed multiple isostructural ($1T$ phase) electronic transition signatures are quite consistent with the above proposed model. Hence, we attribute the isostructural anomalies at ∼2 GPa from XRD, Raman, and resistance to the nontrivial TQPT as a consequence of the predicted band inversion at the A point of the BZ [23]. In this electronic transition, conduction band characters (dominated by Te-p orbitals) are exchanged with valence band characters (dominated by Ti-d orbitals) at A points of the electronic band structure [23]. Similarly, the anomalies at ∼4 GPa may be

due to the trivial metal as a consequence of band inversion at the L point of the BZ. Here, conduction band characters (dominated by Ti-d orbitals) are switched with valence band characters (dominated by Te-p orbitals) at the L points of the electronic band structure [23]. The charge density fluctuations that have occurred during band inversion at the A and L points of the BZ lead to anomalies in c/a ratio at ∼2 GPa and ∼4 GPa, respectively. The charge redistribution modulates the electronic structure and consequently the phonon lifetime is affected, which is reflected as the unusual electron-phonon coupling at ∼2 GPa and ∼4 GPa in Raman linewidth. A small difference exists between the theoretical (0.88 GPa and 3.40 GPa) and experimental (2 GPa and 4 GPa) pressure values. The transition pressure from the result of DFT theory may or may not quantitatively match experimental values due to various approximations used in the theoretical approach. Particularly for the high-pressure experiments, the mismatches between the transition pressure values are reported in the literature. For instance, different theoretical calculations predict the transition pressure of band inversion in Sb_2Se_3 at ∼1 GPa and ∼2 GPa; however, experimentally sharp Raman anomalies are found at ∼2.5 GPa [5,11]. Similarly, using the local density approximation (LDA) and generalized gradient approximation (GGA), the topological phase transition points are found to be 1.7 GPa (LDA) and 4.1 GPa (GGA) for the BiTeI compound, but the experimentally obtained transition point is ∼2.0–2.9 GPa [3,9]. The above examples illustrate the mismatch between the theoretical and experimental transition pressure values, which are quite commonly observed due to the approximation used in theory. However we have seen two isostructural electronic transitions at ∼2.0 GPa and ∼4 GPa within the stability of the trigonal structure of $TiTe_2$ and the transition pressure values quite closely agree with the theoretical predictions (∼0.88 GPa and 3.40 GPa) [23].

Like TQPT, the anomalous changes in Raman linewidth, pressure coefficient of phonon modes, c/a ratio, and resistivity are indicators for ETT and have been reported for many compounds [47,49–51,58]. Though TQPT and ETT are the two completely different phenomena, experimental signatures (indirect) of the XRD and Raman are quite similar. The common method to distinguish between them (TQPT and ETT) is through electronic band structure, Fermi surface, and topological invariant Z_2 calculation. The ambient 3D topological insulators such as Bi_2Se_3, Bi_2Te_3, and Sb_2Te_3 show ETT under a hydrostatic pressure regime of ∼3−5 GPa [51,58]. In some cases such as black phosphorous and Sb_2Se_3, ETT and TQPT occur together at the same pressure region [11,63]. Our result closely (qualitatively) agrees with the theoretical prediction of TQPT. Also, the possibility of an ETT occurrence for 1T-$TiTe_2$ under pressure is discussed above (theoretical sections). The detailed band topology calculations suggest that there is no possibility of ETT at ∼2 GPa and ∼4 GPa for 1T-$TiTe_2$. Further, the theoretically observed anomaly around 9 GPa (close to experimental value ∼8 GPa), as evidenced by both the Fermi surface topology change and DOS plots, suggests the ETT. Hence, the anomalies at ∼8 GPa are not only associated with the structural transition; they might also be a coexistence of structural phase transition and ETT.

The DFT-based first-principles theoretical calculations support the stability of structural symmetry ($P\bar{3}m1$) of 1T-$TiTe_2$ up to 30 GPa (hydrostatic pressure) [23,34]. But our experimental results contradict these theoretical proposals and show the structural transformation of 1T-$TiTe_2$ from trigonal ($P\bar{3}m1$) to monoclinic ($C2/m$) at ∼8 GPa under hydrostatic pressure. One point to note here is that the experiment shows the coexistence of two phases consisting of both the ground-state structure ($P\bar{3}m1$) and the high-pressure structure ($C2/m$) from 8 GPa to 16 GPa (highest pressure reached in this study); still the transformation remains incomplete. It is to be mentioned that present calculations [23,34] (including our theoretical work) may not validate such a coexistence of two phases and that could be one of the reasons why theory could not capture the structural transition at 8 GPa. It is noteworthy that this kind of coexistence of two phases over large pressure regions has been observed in the prototype system $IrTe_2$ [40].

This pressure-induced structural transition may be limiting the detection of two other theoretically predicted electronic transitions at higher pressure regions ∼10.7 GPa and ∼26.4 GPa (beyond the pressure range explored in this work) in the $P\bar{3}m1$ phase. Moreover, as the pressure increases, the $TiTe_2$ sample becomes more and more metallic, which is consistent with the overall intensity reduction of the phonon modes in Raman measurement. This pressure-enhanced metallization could mainly be due to the following two physical reasons. (1) The pressure decreases the interlayer Te(1)-Te(2) contact distance and van der Waals interactions and hence bridges the two layers at ∼4 GPa onwards. (2) In the intralayer, electron transfer from the p orbitals of the Te atom to d orbitals of the Ti atom increases under pressure. This is confirmed by our first-principles calculations, which show that the applied hydrostatic pressure bridges the interlayer Te(1) and Te(2) via the charge density redistributions which results in the conversion of an anisotropic 2D to isotropic 3D behavior at the pressure range from 4 GPa to 8 GPa (1T phase).

Raman anomalies in the 1T-$TiTe_2$ compound can be addressed by considering the anharmonic approximations [11] in the phonon dispersion calculations as a function of pressure which is computationally expensive and beyond the scope of the present work. In addition, for this purpose, the insight of the experimentally observed additional mode (zone-folded mode M) may be needed, and hence nonadiabatic phonon renormalization computational studies can be taken as a separate future work. In consideration of our multiple experimental signatures such as charge density fluctuations, transport anomalies, and unusual electron-phonon coupling at ∼2 GPa and ∼4 GPa with the close agreement of the theoretically proposed the model [23], we attribute these to topologically nontrivial and trivial transitions at ∼2 GPa and ∼4 GPa, respectively. Also, we would like to recall and emphasize that similar indirect experimental signatures (Raman, XRD, and electrical transport) combined with first-principles calculations have been claimed as topologically nontrivial (or band inversion) properties in various systems such as BiTeI, Sb_2Se_3, BiTeBr, and black phosphorous [9–11,63]. Hence, we hope our experimental signatures of anomalies in phonon linewidth, c/a ratio, and transport for 1T-$TiTe_2$ will stimulate research interest towards this material on the aspect of TQPT using a more sophisticated direct tool such as Shubnikov–de Haas oscillation under pressure and provide further insight.

VI. CONCLUSIONS

In conclusion, systematic pressure-dependent synchrotron XRD, Raman, and electrical resistance studies were carried out on $1T$-$TiTe_2$ samples up to ~16 GPa. We observe a first-order structural phase transition at ~8 GPa from trigonal ($P\bar{3}m1$) to monoclinic ($C2/m$) symmetry. The pressure-dependent c/a ratio and electrical resistance show anomalies at ~2 GPa and ~4 GPa in the $1T$ phase which suggests charge density fluctuations upon compression. This is consistent with the phonon linewidth anomalies at ~2 GPa and ~4 GPa indicating unusual electron-phonon coupling arising from the electronic structure changes under pressure. These multiple experimental signatures of the two isostructural electronic transitions at ~2 GPa and ~4 GPa are closely consistent with the theoretical predictions and hence may be due to nontrivial TQPT and trivial metallic transition, respectively. The 2D layered crystal of $TiTe_2$ (at ambient condition) switched into a quasi-3D network above 4 GPa via shortening of the interlayer Te(1)-Te(2) contact distances by external hydrostatic pressure inducing strains, which could be the precursor for the structural transition observed at ~8 GPa. The pressure evolution of the calculated band structure and Fermi surface shows that there is an occurrence of an ETT at ~9 GPa (close to experimental value ~8 GPa) in the $1T$ phase. We hope our experimental finding will stimulate researchers to further explore this $1T$-$TiTe_2$ compound from the aspect of quantum oscillation measurement such as the Shubnikov–de Haas effect under pressure.

ACKNOWLEDGMENTS

We acknowledge the Department of Science and Technology (DST), India, for supporting us financially to carry out XRD measurements at the Xpress beam line, Elettra Synchrotron, Trieste, Italy. S.C.P. and C.N. acknowledge DST-SERB for the financial support under Grant No. SB/S2/CMP-019/2014. C.N. would like to acknowledge Dr. S. Karmakar of BARC, Mumbai, for helping us with the high-pressure resistance measurements and helping in scientific discussions. B.J. acknowledges IISc Bangalore and ICTP Trieste for support through an IISc-ICTP fellowship. C.N. thanks the Sheikh Saqr Laboratory for support through a Senior Fellowship. P.C.S. and V.K. would like to thank IIT Hyderabad for the computational facility, and P.C.S. would like to thank MHRD for fellowship.

[1] M. Z. Hassan and C. L. Kane, Rev. Mod. Phys. **82**, 3045 (2010).
[2] J. E. Moore, Nature (London) **464**, 194 (2010).
[3] M. S. Bahramy, B. J. Yang, R. Arita, and N. Nagaosa, Nat. Commun. **3**, 679 (2012).
[4] W. Liu, X. Peng, C. Tang, L. Sun, K. Zhang, and J. Zhong, Phys. Rev. B **84**, 245105 (2011).
[5] W. Li, X. Y. Wei, J. X. Zhu, C. S. Ting, and Y. Chen, Phys. Rev. B **89**, 035101 (2014).
[6] S. Y. Xu, Y. Xia, L. A. Wray, S. Jia, F. Meier, J. H. Dil, J. Osterwalder, B. Slomski, A. Bansil, H. Lin, R. J. Cava, and M. Z. Hasan, Science **332**, 560 (2011).
[7] T. Sato, K. Segawa, K. Kosaka, S. Souma, K. Nakayama, K. Eto, T. Minami, Y. Ando, and T. Takahashi, Nat. Phys. **7**, 840 (2011).
[8] P. Dziawa, B. J. Kowalski, K. Dybko, R. Buczko, A. Szczerbakow, M. Szot, E. Łusakowska, T. Balasubramanian, B. M. Wojek, M. H. Berntsen, O. Tjernberg, and T. Story, Nat. Mater. **11**, 1023 (2012).
[9] X. Xi, C. Ma, Z. Liu, Z. Chen, W. Ku, H. Berger, C. Martin, D. B. Tanner, and G. L. Carr, Phys. Rev. Lett. **111**, 155701 (2013).
[10] A. Ohmura, Y. Higuchi, T. Ochiai, M. Kanou, F. Ishikawa, S. Nakano, A. Nakayama, Y. Yamada, and T. Sasagawa, Phys. Rev. B **95**, 125203 (2017).
[11] A. Bera, K. Pal, D. V. S. Muthu, S. Sen, P. Guptasarma, U. V. Waghmare, and A. K. Sood, Phys. Rev. Lett. **110**, 107401 (2013).
[12] Y. L. Chen, J. G. Analytis, J. H. Chu, Z. K. Liu, S. K. Mo, X. L. Qi, H. J. Zhang, D. H. Lu, X. Dai, Z. Fang, S. C. Zhang, I. R. Fisher, Z. Hussain, and Z. X. Shen, Science **325**, 178 (2009).
[13] D. Hsieh, Y. Xia, L. Wray, D. Qian, A. Pal, J. H. Dil, J. Osterwalder, F. Meier, G. Bihlmayer, C. L. Kane, Y. S. Hor, R. J. Cava, and M. Z. Hasan, Science **323**, 919 (2009).
[14] Yu. S. Ponosov, T. V. Kuznetsova, O. E. Tereshchenko, K. A. Kokh, and E. V. Chulkov, JETP Lett. **98**, 557 (2013).
[15] P. P. Kong, F. Sun, L. Y. Xing, J. Zhu, S. J. Zhang, W. M. Li, Q. Q. Liu, X. C. Wang, S. M. Feng, X. H. Yu, J. L. Zhu, R. C. Yu, W. G. Yang, G. Y. Shen, Y. S. Zhao, R. Ahuja, H. K. Mao, and C. Q. Jin, Sci. Rep. **4**, 6679 (2014).
[16] K. Saha, K. Légaré, and I. Garate, Phys. Rev. Lett. **115**, 176405 (2015).
[17] Y. Chen, X. Xi, W. Yim, F. Peng, Y. Wang, H. Wang, Y. Ma, G. Liu, C. Sun, C. Ma, Z. Chen, and H. Berger, J. Phys. Chem. C **117**, 25677 (2013).
[18] J. Park, K. H. Jin, Y. J. Jo, E. S. Choi, W. Kang, E. Kampert, J. S. Rhyee, S. H. Jhi, and J. S. Kim, Sci. Rep. **5**, 15973 (2015).
[19] I. Efthimiopoulos, J. Zhang, M. Kucway, C. Park, R. C. Ewing, and Y. Wang, Sci. Rep. **3**, 2665 (2013).
[20] T. E. Kidd, T. Miller, M. Y. Chou, and T.-C. Chiang, Phys. Rev. Lett. **88**, 226402 (2002).
[21] A. F. Kusmartseva, B. Sipos, H. Berger, L. Forro, and E. Tutis, Phys. Rev. Lett. **103**, 236401 (2009).
[22] J. Khan, C. M. Nolen, D. Teweldebrhan, D. Wickramaratne, R. K. Lake, and A. A. Balandin, Appl. Phys. Lett. **100**, 043109 (2012).
[23] Q. Zhang, Y. Cheng, and U. Schwingenschlogl, Phys. Rev. B **88**, 155317 (2013).
[24] J. C. Chervin, B. Canny, and M. Mancinelli, High Pressure Res. **21**, 305 (2001).
[25] S. Klotz, J. C. Chervin, P. Munsch, and G. L. Marchand, J. Phys. D: Appl. Phys. **42**, 075413 (2009).
[26] A. P. Hammersley, S. O. Svensson, M. Hanfland, A. N. Fitch, and D. Häusermann, High Pressure Res. **14**, 235 (1996).
[27] S. J. Clark, M. D. Segall, C. J. Pickard, P. J. Hasnip, M. I. J. Probert, K. Refson, and M. C. Payne, Z. Kristallogr. Cryst. Mater. **220**, 567 (2005).
[28] P. Blaha, K. Schwarz, G. K. H. Madsen, D. Kvasnicka, and J. Luitz, *WIEN2k, An Augmented Plane Wave + Local Orbitals*

Program for Calculating Crystal Properties, edited by K. Schwarz (Techn. Universitat Wien, Austria, 2001).
[29] T. H. Fischer and J. Almlof, J. Phys. Chem. **96**, 9768 (1992).
[30] J. P. Perdew, K. Burke, and M. Ernzerhof, Phys. Rev. Lett. **77**, 3865 (1996).
[31] C. Riekel, M. Thomas, and R. Schollhorn, Phys. Status Solidi A **50**, K231 (1978).
[32] Y. Arnaud and M. Chevreton, J. Solid State Chem. **39**, 230 (1981).
[33] H. Ding and B. Xu, J. Chem. Phys. **137**, 224509 (2012).
[34] R. C. Xiao, W. J. Lu, D. F. Shao, J. Y. Li, M. J. Wei, H. Y. Lv, P. Tong, X. B. Zhu, and Y. P. Sun, J. Mater. Chem. C **5**, 4167 (2017).
[35] M. Hangyo, S. I. Nakashima, and A. Mitsuishi, Ferroelectrics **52**, 151 (1983).
[36] P. Goli, J. Khan, D. Wickramaratne, R. K. Lake, and A. A. Balandin, Nano Lett. **12**, 5941 (2012).
[37] R. Samnakay, D. Wickramaratne, T. R. Pope, R. K. Lake, T. T. Salguero, and A. A. Balandin, Nano Lett. **15**, 2965 (2015).
[38] O. R. Albertini, R. Zhao, R. L. McCann, S. Feng, M. Terrones, J. K. Freericks, J. A. Robinson, and A. Y. Liu, Phys. Rev. B **93**, 214109 (2016).
[39] See Supplemental Material at http://link.aps.org/supplemental/10.1103/PhysRevB.97.085107 for additional experimental (XRD, Raman, and resistance measurements) and theoretical information.
[40] J. M. Leger, A. S. Pereira, J. Haines, S. Jobic, and R. Brec, J. Phys. Chem. Solids **61**, 27 (2000).
[41] M. Hiue, Y. Akahama, M. Kobayashi, and H. Kawamura, Rev. High Pressure Sci. Technol. **7**, 344 (1998).
[42] J. R. Carvajal, Phys. B **192**, 55 (1993).
[43] A. Boultif and D. Lour, J. Appl. Cryst. **24**, 987 (1991).
[44] F. D. Murnaghan, Proc. Natl. Acad. Sci. U.S.A. **30**, 244 (1944).
[45] F. Birch, Phys. Rev. **71**, 809 (1947).
[46] Z. Zhao, H. Zhang, H. Yuan, S. Wang, Y. Lin, Q. Zeng, G. Xu, Z. Liu, G. K. Solanki, K. D. Patel, Y. Cui, H. Y. Hwang, and W. L. Mao, Nat. Commun. **6**, 7312 (2015).
[47] R. Vilaplana, D. S. Perez, O. Gomis, F. J. Manjon, J. Gonzalez, A. Segura, A. Munoz, P. R. Hernandez, E. P. Gonzalez, V. M. Borras, V. M. Sanjose, C. Drasar, and V. Kucek, Phys. Rev. B **84**, 184110 (2011).
[48] M. Cardona, High Pressure Res. **24**, 17 (2004).
[49] Y. A. Sorb, V. Rajaji, P. S. Malavi, U. Subbarao, P. Halappa, S. C. Peter, S. Karmakar, and C. Narayana, J. Phys.: Condens. Matter **28**, 015602 (2016).
[50] V. Rajaji, P. S. Malavi, S. S. R. K. C. Yamijala, Y. A. Sorb, U. Dutta, S. N. Guin, B. Joseph, S. K. Pati, S. Karmakar, K. Biswas, and C. Narayana, Appl. Phys. Lett. **109**, 171903 (2016).
[51] F. J. Manjon, R. Vilaplana, O. Gomis, E. P. Gonzalez, D. S. Perez, V. M. Borras, A. Segura, J. Gonzalez, P. R. Hernandez, A. Munoz, C. Drasar, V. Kucek, and V. M. Sanjose, Phys. Status Solidi B **250**, 669 (2013).
[52] M. L. Doublet, N. G. Planas, P. H. T. Philipsen, R. Brec, and S. Jobic, J. Chem. Phys. **108**, 648 (1998).
[53] E. Canadell, S. Jobic, R. Brec, J. Rouxel, and M. H. Whangbo, J. Solid State Chem. **99**, 189 (1992).
[54] Y. Koike, M. Okamura, T. Nakanomyo, and T. Fukase, J. Phys. Soc. Jpn. **52**, 597 (1983).
[55] D. K. G. de Boer, C. F. van Bruggen, G. W. Bus, R. Coehoorn, C. Haas, G. A. Sawatzky, H. W. Myron, D. Norman, and H. Padmore, Phys. Rev. B **29**, 6797 (1984).
[56] G. Fritscht, W. Dyckhoff, W. Pollich, and E. Liischer, J. Phys. F: Met. Phys. **15**, 1537 (1985).
[57] Y. Ding, C. C. Chen, Q. Zeng, H. S. Kim, M. J. Han, M. Balasubramanian, R. Gordon, F. Li, L. Bai, D. Popov, S. M. Heald, T. Gog, H. K. Mao, and M. van Veenendaal, Phys. Rev. Lett. **112**, 056401 (2014).
[58] J. Zhang, C. Liu, X. Zhang, F. Ke, Y. Han, G. Peng, Y. Ma, and C. Gao, Appl. Phys. Lett. **103**, 052102 (2013).
[59] J. Zhao, L. Yang, Z. Yu, Y. Wang, C. Li, K. Yang, Z. Liu, and Y. Wang, Inorg. Chem. **55**, 3907 (2016).
[60] E. Greenberg, B. Hen, S. Layek, I. Pozin, R. Friedman, V. Shelukhin, Y. Rosenberg, M. Karpovski, M. P. Pasternak, E. Sterer, Y. Dagan, G. Kh. Rozenberg, and A. Palevski, Phys. Rev. B **95**, 064514 (2017).
[61] I. M. Lifshitz, Sov. Phys. JETP **11**, 1130 (1960).
[62] S. Ram, V. Kanchana, G. Vaitheeswaran, A. Svane, S. B. Dugdale, and N. E. Christensen, Phys. Rev. B **85**, 174531 (2012).
[63] S. N. Gupta, A. Singh, K. Pal, B. Chakraborti, D. V. S. Muthu, U. V. Waghmare, and A. K. Sood, Phys. Rev. B **96**, 094104 (2017).